Bi_2S_3/rGO nanocomposites with covalent heterojunctions as a high-performance aqueous zinc ion battery material

Shaohua Zhang, [1,2+] Chun Lin,[1,2+] Jiefeng Ye,[1,3] Dongni Zhao,[5,6] Yue Chen,[1,4,6 *] Jian-Min Zhang, [1,3 *] Jianmin Tao, [1,2] Jiaxin Li,[1,2] Yingbin Lin,[1,2] Stijn F. L. Mertens,[5,6] Oleg V. Kolosov,[4,6] and Zhigao Huang[1,3 *]

[1]*College of Physics and Energy, Fujian Normal University, Fujian Provincial Key Laboratory of Quantum Manipulation and New Energy Materials, Fuzhou, 350117, China*

[2]*Fujian Provincial Engineering Technical Research Centre of Solar-Energy Conversion and Stored Energy, Fuzhou, 350117, China*

[3]*Fujian Provincial Collaborative Innovation Centre for Advanced High-Field Superconducting Materials and Engineering, Fuzhou, 350117, China*

[4]*Department of Physics, Lancaster University, Lancaster, LA1 4YB, UK*

[5]*Department of Chemistry, Energy Lancaster and Materials Science Institute, Lancaster LA1 4YB, UK*

[6]*The Faraday Institution, Harwell Science and Innovation Campus, OX11 0RA, Didcot, UK*

Corresponding authors: y.chen102@lancaster.ac.uk; jmzhang@fjnu.edu.cn; zghuang@fjnu.edu.cn

S. Z.[+] and C. L.[+] contributed equally.

Abstract:

Bismuth(III) sulfide (Bi_2S_3) is a promising cathode material for aqueous zinc ion batteries (ZIBs), yet suffers from serious capacity issues due to its poor electrical conductivity and microstructural degradations. In this work, Bi_2S_3 anchored on reduced graphene oxide (rGO) is prepared through hydrothermal reaction and is used as cathode material for aqueous ZIBs. Raman and XPS characterizations confirmed that the oxygen bridge in Bi-O-C heterostructures is successfully created during the hydrothermal synthesis. These oxygen bridges are energy favourable in the Bi_2S_3/rGO composite materials and serve as the electron transfer channels for rapid charge compensation during Zn^{2+} incorporation/extraction. Rotating ring–disc electrode (RRDE) measurements demonstrate improved electrochemical stability of the Bi_2S_3/rGO composite material compared to pristine Bi_2S_3. As a result of these improved characteristics, Bi_2S_3/rGO composite shows notably better rate performance and cycling stability than unsupported Bi_2S_3. *Ex-situ* X-ray diffraction and XPS

characterizations indicate that Zn^{2+} undergoes a reversible conversion reaction with Bi_2S_3 to form ZnS/Bi^0, rather than being intercalated into Bi_2S_3 crystal interlayers. The rGO substrate forms chemical bonds with bismuth in the composite material, and the strongly anchored bismuth on the rGO through a Bi-O-C bridge enables a highly reversible conversion reaction. As a result, the Bi_2S_3/rGO composite with 8 wt.% rGO can deliver a reversible capacity of ~186 mAh g^{-1} at the current density of 500 mA g^{-1} after 150 cycles, showing high promise as Zn-ion battery material.

Keywords: Aqueous Zn-ion batteries; Bi_2S_3; rGO conductive network; charge storage mechanism.

1. Introduction

Lithium-ion batteries (LIBs) have been widely used in everyday electric equipment, electric vehicles and energy storage systems [1-5]. Recently, the supply of lithium mineral resources has been unstable [6], and the price of Li_2CO_3 resources for LIBs has doubled in the past few years due to the global pandemic and geopolitical instability. The shortage of lithium resources, recycling sustainability and the safety issues of lithium-ion batteries has driven scientists to search for alternative energy storage devices. As a result, with rich zinc natural resources, its environmental friendliness and safety, aqueous zinc ion batteries (ZIBs) are attracting increasing attention [7].

The limited choice of cathode materials hinders the development of advanced high-energy-density aqueous ZIBs. At present, manganese oxide [8-10] and vanadium oxide [11-13] are the two most widely studied cathode materials for ZIBs, but these materials have a common disadvantage, that is, the migration of Zn^{2+} in these materials is limited by the strong electrostatic interaction with lattice oxygen ions. The strong electrostatically "bonded" Zn^{2+} cannot be completely removed from the lattice of the active material during the charging process, resulting in poor reversible capacity. To reduce the strong electrostatic interaction between Zn^{2+} and O^{2-} in metal oxides [14,15], an effective strategy is to replace lattice oxides with sulfur. In other words, compared with metal oxides, metal sulfides with anionic substitution from O^{2-} to S^{2-} may effectively improve the electrochemical performance and reversibility of ZIBs.

As a promising type of battery material, metal sulfides with layered structures have been extensively

studied and applied in monovalent (Li^+, Na^+, K^+) rechargeable batteries [16]. Although there have been some studies of Bi_2S_3 [17], MoS_2 [18], V_5S_8 [19] and SeS_2 [20] as ZIB material, the detailed electrochemical charge storage and transfer mechanisms of these metal sulfides have not been comprehensively understood yet. For example, Bi_2S_3 has a layered structure in which the highly anisotropic Bi-S layer is combined by weak van der Waals interaction, which may provide the channels for the insertion and extraction of foreign ions [17,21,22]. However, Zhi et al. suggested that Bi_2S_3 undergoes a conversion reaction by replacing the Bi^{2+} with Zn^{2+} (single-displacement reaction) during the charge/discharge [23]. Considering that Bi_2S_3 is a semiconductor material with a narrow band gap of 1.3 eV, its poor intrinsic conductivity, together with its sluggish reaction dynamics and lattice expansion, have become major obstacles to further enhancing its electrochemical performance and charge/discharge cycle stability [24]. To tackle these problems, Gao *et al.* [25] prepared Bi_2S_3@CNT nanocomposites, in which carbon nanotubes (CNT) conductive network promoted electron transport, delivering 84.4 mAh g^{-1} capacity at a current density of 60 mA g^{-1} as a sodium ion electrode material. Similarly, Sun [26] *et al.* designed a three-dimensional nitrogen-doped graphene framework with encapsulated Bi_2S_3 nanorods to improve the conductivity of the composite material. These previous reports on "Bi_2S_3/carbon-network" composite materials all demonstrated high reversible capacity and good cycling performance as a lithium/sodium ion battery anode [21,22,24-26]. However, there are few reports on the study of electrochemical performance and energy storage mechanism of Bi_2S_3 as a potential active material in aqueous ZIBs.

Inspired by the above research, Bi_2S_3 and reduced graphene oxide (rGO) composites were prepared by hydrothermal reaction in this study. The optimized Bi_2S_3-rGO composite can deliver an initial charge capacity of 313 mAh g^{-1} at a current density of 100 mA g^{-1}, which is much higher than the neat Bi_2S_3 electrode without rGO additive. Based on *ex-situ* XRD and XPS data, we ascribe the Zn storage mechanism in the Bi_2S_3/rGO composite to a conversion reaction. The improved electrochemical performance in Bi_2S_3/rGO, including rate performance and reversibility, is attributed to the flexible conductive network constructed by rGO and the Bi-O-C covalent bonds that strongly anchor bismuth on the graphene.

2. Experimental section

2.1 Material Preparation and Characterization

Bi_2S_3/rGO composites were synthesized by hydrothermal method. The details and schematic diagram of Bi_2S_3/rGO composite material preparation are shown in Supplementary Information, SI, Figure S1. Bismuth nitrate pentahydrate ($Bi(NO_3)_3)\cdot 5H_2O$ and sodium thiosulfate ($Na_2S_2O_3$) were used as bismuth and sulfur source, respectively, to dissolve and mix with graphene oxide (GO). Glucose was added to the mixed solution to inhibit the formation of impurities in the hydrothermal product [27] (Figure S2). The mixed solution was stirred for 2 hours to obtain a uniform mixture and then transferred to a Teflon/stainless steel autoclave and heated at 180 ℃ for 24 hours. The precipitate was collected, placed in a tubular furnace, and heated to 400 ℃ for 3 hours in a high-purity argon (99.999%) atmosphere. To determine the effect of the mass ratio between Bi_2S_3 and rGO on the structure and properties, the composite was prepared by adjusting the wt. % of rGO from 4%, 8% to 12%, and the final products were denoted as Bi_2S_3-rGO4, Bi_2S_3-rGO8, and Bi_2S_3-rGO12. Powder X-ray diffraction (XRD) (Rigaku MinFlex II, Cu-Kα, λ=1.5406 A) and Transmission Electronic Microscopy (TEM) (Titan, FEI) were used to investigate the crystal structure of the samples. Raman spectrometry (LabRam HR Evolution) was used to quantify the defects and identify chemical bonds in the composite. Field emission scanning electron microscope (SEM, HITACHI, SU-8010) equipped with an energy dispersive spectrometer (EDS) was used to study particle morphology and the change of material surface morphology at different charge and discharge states. X-ray photoelectron spectroscopy (XPS, Thermo Scientific ESCALAB 250Xi) was used to analyze the surface chemistry of materials.

2.2 Electrochemical Characterization

The electrochemical performance of Bi_2S_3/rGO composite electrodes was tested in coin cells (CR-2025 type). The electrode was prepared by mixing 70 wt.% active material, 20 wt.% Super P, 10 wt.% polyvinylidene fluoride, then the mixed slurry was coated on the stainless-steel foil after cleaning with anhydrous ethanol and dried in a vacuum oven at 80℃ for 12 hours. Glass fiber (Whatman) and zinc foil were used as the separator and anode, respectively, and 2 M $ZnSO_4$ aqueous solution was used as the electrolyte. The cell was activated by two cycles with a small current of 100 mA g^{-1}. The LAND test system (CT2001A) was used to conduct constant current charge and discharge tests at different

current densities, with the voltage range of charge and discharge from 0.2 V to 1.4 V vs Zn anode. Cyclic voltammetry (CV) test was carried out in an electrochemical workstation (CHI 760E), and the CV curves of the materials were tested at the sweep rates of 0.2 mV s^{-1}, 0.4 mV s^{-1}, 0.6 mV s^{-1}, 0.8 mV s^{-1} and 1 mV s^{-1}. Electrochemical impedance spectroscopy (EIS) of the battery was recorded on the Zahner Zennium IM6 electrochemical workstation with a frequency range of 100 mHz to 100 kHz and an AC amplitude of 5 mV.

For preparing the rotating ring–disc electrode (RRDE), 70 wt.% active material, 20 wt.% Super P, 10 wt.% polyvinylidene fluoride were dispersed in dimethylsulfoxide (DMSO, reagent grade) to form the electrode slurry. The mixture was sonicated for 30 minutes and shaken in a vortex mixer (Vortex Genie 2, Scientific Industries) for 5 minutes and then evenly coated on the disc electrode. The RRDE system with a modulated speed rotator (AFMSRCE, Pine Research) and an interchangeable RRDE was set up for active materials dissolution detection. The RRDE consists of a glassy carbon (GC) disc (OD=5.0 mm) and a platinum (Pt) ring (ID=6.5 mm, OD=7.5 mm). The geometric electrode area of the disc and ring is 0.196 cm^2 and 0.110 cm^2, respectively, and the collection efficiency for this RRDE is around 0.25. The electrode dissolution was detected with a rotating speed of 1600 RPM in this study. A Leak-Free Ag/AgCl/3.4 M KCl electrode (Innovative Instruments) and a Pt coil were used as reference and counter electrodes, respectively. Potentials were converted to the Zn^{2+}/Zn scale using the equation *E vs* Zn^{2+}/Zn = 0.959 V + *E vs* Ag/AgCl. The voltammograms and chronoamperograms of the RRDE were recorded by a Biologic SP-300 potentiostat. During cyclic voltammetry (CV) of Bi_2S_3 and Bi_2S_3/rGO, a scan rate of 10 mV/s was used, and the Pt ring was held at 0.1 V vs Ag/AgCl. Before drop-casting 9 µL of the electrode slurry onto the GC disc, the RRDE was polished with 0.1 and 0.05 µm alumina suspension (Buehler) and rinsed with ultrapure water (MilliQ, Millipore, 18.2 MOhm cm, total organic carbon < 2 ppb). The electrode was then dried at room temperature under a low vacuum overnight. 0.2 M $ZnSO_4$ was used as the electrolyte, which was prepared by diluting 2.0 M $ZnSO_4$ (BioUltra, Merck) with ultrapure water.

2.3 Density Functional Theory (DFT) calculation

In this work, the rGO/Bi_2S_3 heterojunction behaviour was theoretically calculated based on density functional theory (DFT), using a projected augmented wave (PAW) [28] method implemented in the

Vienna *ab initio* simulation package (VASP) [29,30]. The generalized gradient approximation (GGA) [31] at the level of Perdew–Burke–Ernzerhof (PBE) was treated as the electron exchange-correlation functional. A 2×1×1 Bi_2S_3 supercell was constructed to be the base. The space group of *Pnma* (No. 62) and the lattice constants are a = 4.02 Å, b = 11.17 Å and c = 11.74 Å. The rGO consisted of a 3×3 graphene supercell with hydrogen and oxygen atoms surrounding it, which was adsorbed to Bi_2S_3 along the a-axis. The plane-wave basis cut-off energy was set to 520 eV. The geometric optimization would not be completed until the total energy converged to 10^{-5} eV and the maximum residual force acting on each atom was less than 0.01 eV/Å. A vacuum layer of 20 Å in a direction is added. The sampling of Brillouin zone was performed with a 3×3×1 k-point grid by the Monkhorst-Pack method [32]. The dispersion-corrected density functional theory optB88-vdW [33] was employed to calculate the interlayer binding energy.

3. Results and discussion

3.1 Structure characterizations of Bi_2S_3 and Bi_2S_3/rGO composites

Figure 1(a) shows the XRD patterns of Bi_2S_3 and Bi_2S_3/rGO materials, all diffraction peaks in the pattern belong to rhombic Bi_2S_3 with *Pbnm*(62) space group symmetry. The diffraction peaks belonging to Bi_2S_3 are sharp, indicating that the as-prepared bismuth sulfide sample has high crystallinity. For the Bi_2S_3/rGO composites, no additional diffraction peak of graphitic carbons is detected. The absence of a carbon (002) peak in Bi_2S_3/rGO also indicates that rGO is rarely aggregated as graphitic carbons during the hydrothermal process and annealing process [34]. Meanwhile, the intensity of diffraction peaks of Bi_2S_3/rGO composites decreases with increasing rGO content, while the full width at half maximum (FWHM) increases compared with the bare Bi_2S_3. The reason for this is that with increasing rGO wt%, higher availability of nucleation sites in rGO results in the reduced grain size of Bi_2S_3; conversely, the growth of layered Bi_2S_3 on the graphene surface facilitates the dispersion of graphene [35].

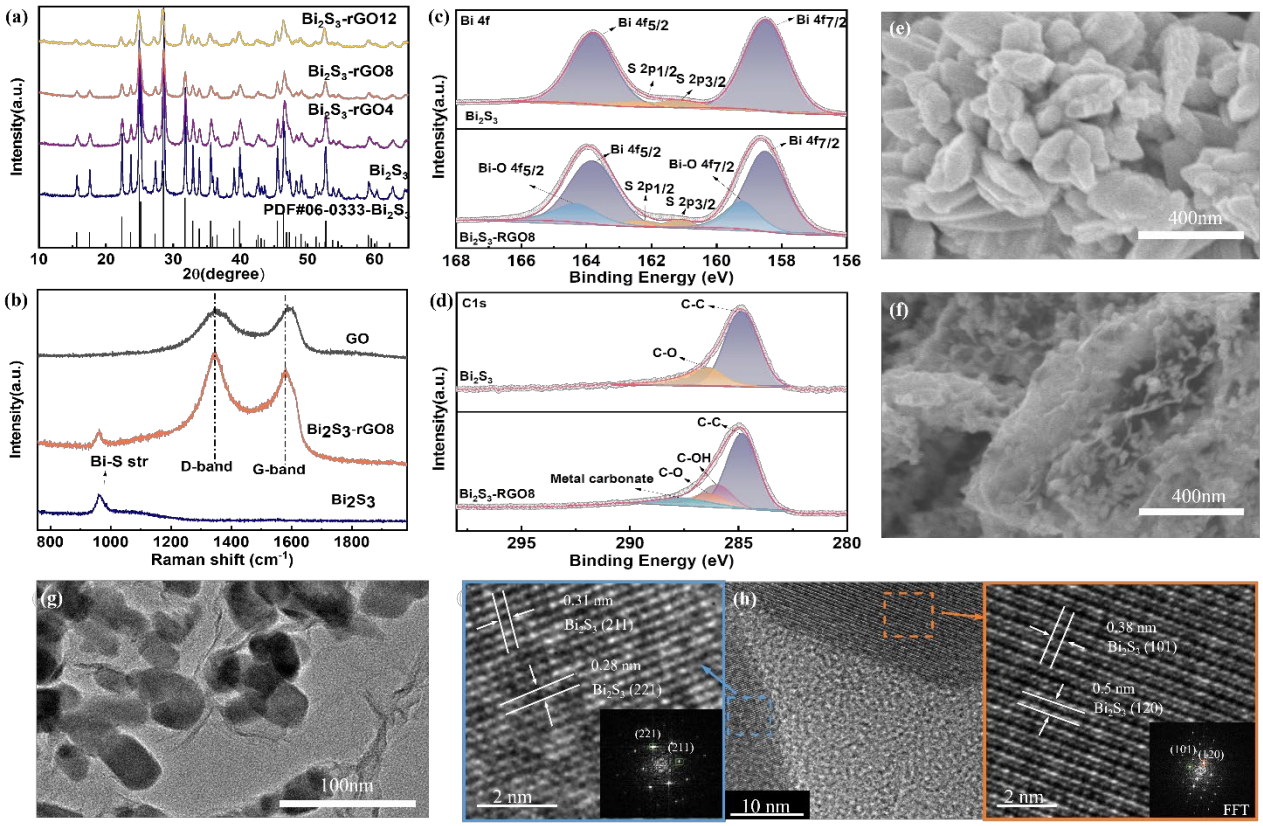

Figure 1. (a) XRD patterns of Bi_2S_3, Bi_2S_3-RGO4, Bi_2S_3-RGO8 and Bi_2S_3-RGO12. (b) Raman spectra of GO, Bi_2S_3-RGO8 and Bi_2S_3. XPS spectra of Bi_2S_3 and Bi_2S_3-RGO8 composite, (c) Bi 4f XPS spectra and (d) C 1s XPS spectra. SEM images of Bi_2S_3 (e) and Bi_2S_3-RGO8 (f). (g-h) High-resolution TEM images of Bi_2S_3-RGO8 sample.

To understand the chemical binding between Bi_2S_3 and rGO, Raman measurements were performed, Figure 1(b). The Raman spectra with varying rGO content can be found in Figure S3. All samples have a peak at 963 cm^{-1}, corresponding to the Bi-S stretch mode of Bi_2S_3 [36]. For the Bi_2S_3-rGO composites, two typical carbon peaks were observed at around 1345 cm^{-1} and 1576 cm^{-1}, corresponding to the D band and the G band respectively. Importantly, compared with the G peak position (~1592 cm^{-1}) of initial GO in Figure 1(b), the peak shifts about 16 cm^{-1} in the Bi_2S_3-rGO composites (~1576 cm^{-1}). This indicates the formation of chemical covalent bonds between the graphene and Bi_2S_3. The reduction of some hydroxide functional groups on the graphene surface, as well as the connection of carbon to the bismuth or sulfide atoms, can both change the G peak vibration frequency of carbon atoms in graphene [37-39].

To further evidence the bonding structures, the XPS spectra of Bi_2S_3 and Bi_2S_3-rGO composites are

compared in Figures 1(c-d). The full survey spectra can be found in Figure S4(a). Figure 2(b) shows the high-resolution spectra of Bi 4f orbit in the two groups of samples. We found that Bi_2S_3 and Bi_2S_3-rGO samples both have two peaks at the binding energies of about 158.5 eV and 163.8 eV, corresponding to the spin-orbit energies of $4f_{5/2}$ and $4f_{7/2}$ of Bi^{3+} in Bi_2S_3 respectively. In addition, there are two peaks in the binding energies of 161.1 eV and 162.3 eV in both samples, corresponding to the spin-orbital energies of the $2p_{3/2}$ and $2p_{1/2}$ of sulfur with a valence state of −2. However, in Bi_2S_3-rGO, two new peaks appear at binding energies of 159.2eV and 164.3eV. These two peaks are attributed to Bi-O bonds derived from the strong chemical bonding between Bi_2S_3 and the reduced functional groups in rGO [38]. Moreover, the C 1s high-resolution spectra shown in Figure 1(d) can be decomposed into four peaks, among which the peak at about 284.8 eV corresponds to sp^3 carbon (C-C), while the peaks at about 285.9 eV, 286.3 eV and 287.7 eV correspond to C-OH, C-O and metal carbonate, respectively. This is due to the different functional groups which were reduced on the surface of rGO [40-42], supporting the existence of Bi_2S_3 and rGO heterostructures (Bi-O-C). This Bi-O-C motif is also consistent with Raman characterization which shows a shift of the G peak in Figure 1(b).

Figures 1(e-f) show SEM images of Bi_2S_3 and Bi_2S_3/rGO composites respectively. As can be seen from Figure 1(e), Bi_2S_3 consists of irregular aggregated nanoparticles with sizes ranging from 50 nm to 300 nm. By contrast, it can be seen from Figure 1(f) that the particle size of Bi_2S_3-rGO8 composites (~30 nm according to the TEM image in Figure S5) is much smaller than that of Bi_2S_3. Furthermore, from the SEM morphology images of bare Bi_2S_3 with different rGO w% in Figure S6, it can be found that the Bi_2S_3 particles were uniformly dispersed on the surface of the graphene film which effectively prevented the agglomeration of Bi_2S_3 nanoparticles by inhibiting the growth of Bi_2S_3. The Bi_2S_3-rGO heterogeneous structure ensures that the material has good electrical contact, and the smaller Bi_2S_3 particle size shortens the diffusion path of Zn^{2+} toward the active material. This structure is confirmed by the TEM image in Figure 1(g), which shows that the Bi_2S_3 nanograins are uniformly dispersed and wrapped by graphene oxide “sheets”. As shown in Figure 1(h), although revealing the detailed crystallographic structure of the heterogeneous Bi_2S_3-rGO is outside the capability of TEM, the well-defined crystal lattice fringes observed in Bi_2S_3 nanograins confirm the good crystallinity, which is consistent with the XRD results in Figure 1(a).

3.2 Electrochemical performance of Bi_2S_3/RGO composite

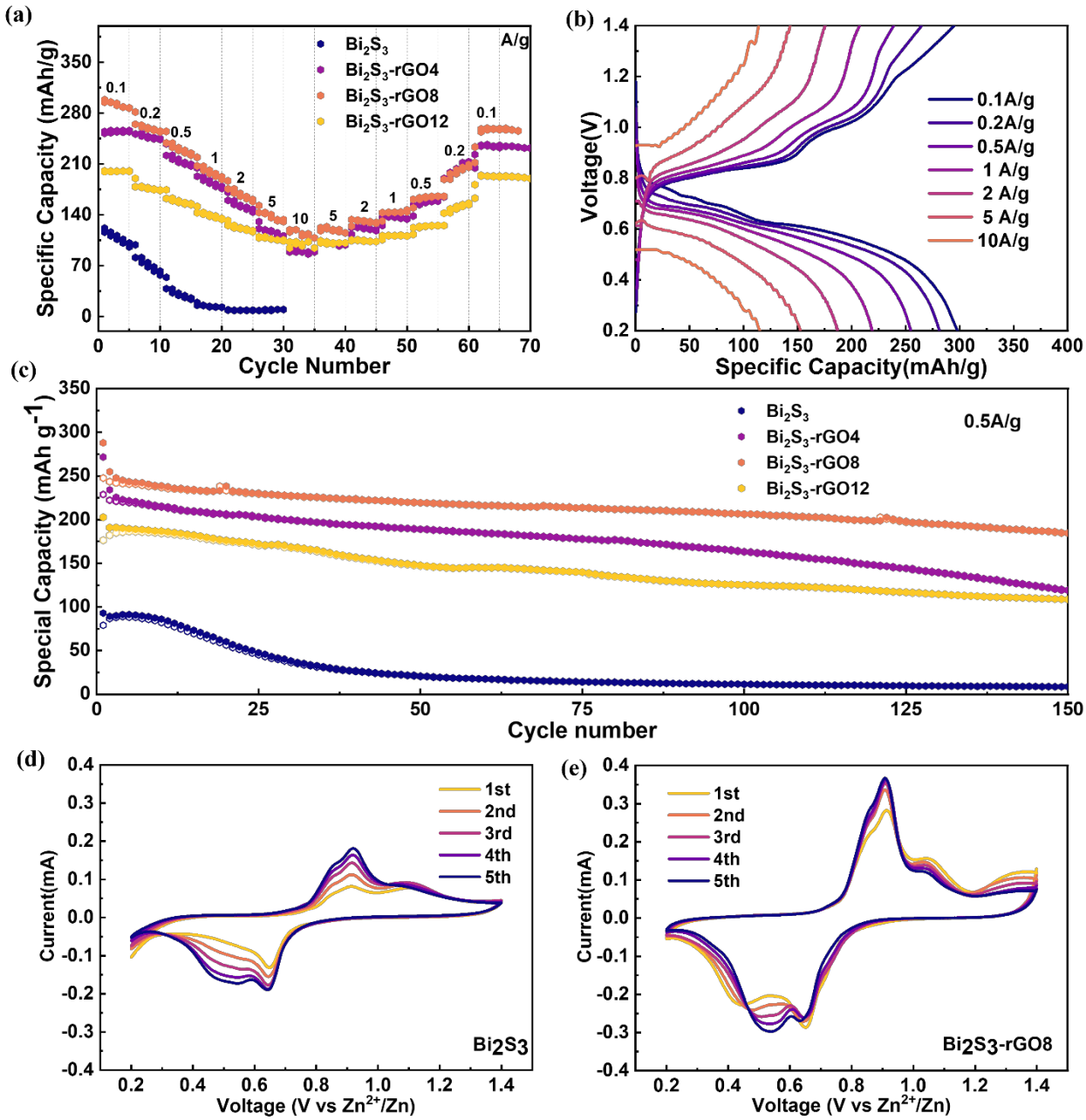

Figure 2. (a) Rate performances in comparison of Bi_2S_3, Bi_2S_3-rGO4, Bi_2S_3-rGO8, and Bi_2S_3-rGO12 under various current densities ranging from 0.1 to 10 A g^{-1}, (b) Galvanostatic charge–discharge curves of Bi_2S_3-rGO8 at different current densities. Long-term cycling stability (c) in comparison of Bi_2S_3, Bi_2S_3-RGO4, Bi_2S_3-rGO8, and Bi_2S_3-rGO12 at 0.5 A g^{-1}. Cyclic voltammograms of (d) Bi_2S_3, (e) Bi_2S_3-rGO8 at 0.1 mV s^{-1}.

Figure 2(a) shows the rate performances of Bi_2S_3 and Bi_2S_3/rGO samples at different current densities from 0.1 to 10 A g^{-1}. Overall, the rate performances of Bi_2S_3-rGO composites are far better than those

of bare Bi_2S_3. Moreover, it is found that Bi_2S_3-rGO8 has the highest specific capacities, 298.3 mAh g^{-1}, 207.4 mAh g^{-1}, and 119.4 mAh g^{-1} at the current density of 0.1 A g^{-1}, 1 A g^{-1}, 10 A g^{-1}, respectively. When the current density is restored to 0.1A g^{-1} after sixty-five cycles, the specific capacity of Bi_2S_3-rGO8 is 255.4 mAh g^{-1}, which is 10-30 % higher than those of Bi_2S_3-rGO4 and Bi_2S_3-rGO12 composites (232.6 and 192.2 mAh g^{-1}). It is well recognized that high current density will damage the microstructure and deactivate the electrode materials []. Bi_2S_3/rGO composite materials can provide excellent rate performance because of their good structural stability. Figure 2(b) shows the charge-discharge curves of Bi_2S_3-rGO8 at different current densities. An inclined discharge platform appears at about 0.53-0.63V and two charging platforms appear at about 0.91V and 1.03V. The voltage platforms even can be observed at the current density of 10 A g^{-1} and the cell can still deliver a reversible capacity of nearly 120 mAh g^{-1}. By contrast, the bare Bi_2S_3 sample delivers only about 8 mAh g^{-1} at the current density of 5 A g^{-1}. With the increase of graphene oxide additive from 4 wt% to 8 wt%, the specific capacity of the electrode gradually increases, and 8 wt% of graphene additive is the most suitable, while excess graphene (12 wt%) will lead to a decrease in the specific capacity. This is because the addition of graphene helps to improve the conductivity of composite materials, and the conductive structure is gradually improved. However, when the amount of graphene added reaches a critical value, the conductivity is no longer improved, but the rGO itself is electrochemically inactive to the Zn ion intercalation and reduces the amount of Bi_2S_3 active material. This is consistent with the best cycle stability of Bi_2S_3-rGO8 as shown in Figure 2(c). We evaluated the long-term cycle performance of the four samples under the current density of 0.5 A g^{-1}. Compared with Bi_2S_3, the Zinc storage performance of Bi_2S_3/rGO composite is significantly improved. The initial specific capacity of Bi_2S_3 electrode is 87.9 mAh g^{-1}, which reduces to 8.3 mAh g^{-1} after 150 cycles, whereas Bi_2S_3-rGO8 electrode has a much better cycling performance among the studied materials. The initial specific capacity of Bi_2S_3-rGO8 electrode is around 254.9 mAh g^{-1}, and it can still deliver a reversible capacity of ~186 mAh g^{-1} after 150 cycles. We believe the origin of a good capacity of Bi_2S_3-rGO8 among all Bi_2S_3/rGO samples is on the small charge transfer resistance which was confirmed by Kelvin probe atomic force microscopy (Figure S7) and electrochemical impedance spectroscopy measurements during the electrochemical cycles (Figure S8). At mid-to-low frequency (0.1-10000 Hz) region of Bode plots as shown in Figure S8, we observed a significantly reduced charge transfer resistance and ion diffusive resistance [44, 45] in Bi_2S_3/rGO8 composite electrode compared with the bare Bi_2S_3

electrode. This reduced impedance at the mid-to-low frequency which well explained the better rate performance of Bi_2S_3/rGO8 composite electrode as shown in Figure 2a. It is also worth noting that the rGO folding was observed after the 10^{th} cycle in Bi_2S_3-rGO8 composite electrode (Figure S9), indicating efforts must be taken into preventing the graphene folding for the further optimization of the cycle stability of Bi_2S_3-rGO8 composite electrode.

Figures 2(d, e) and Figure S10 show cyclic voltammograms (CV) of Bi_2S_3, Bi_2S_3-rGO4, Bi_2S_3-rGO8 and Bi_2S_3-rGO12 samples measured in the first five cycles at a scan rate of 0.1 mV s^{-1}. It can be seen from the figures that all electrode materials have two oxidation peaks and two reduction peaks, which can be attributed to the interaction/de-intercalation between Zn^{2+} and Bi_2S_3 or the reversible reduction of Zn^{2+} forming metallic Zinc [45,46]. The positions of the redox peaks of the four samples are similar, the oxidation peak positions are at about 0.91 V and 1.03 V and the reduction peak is at about 0.53-0.63 V. These oxidation/reduction peaks are consistent with the charging and discharging platforms in Figure 2(b). Meanwhile, we observed that the intensity of the redox peaks of Bi_2S_3 electrodes is gradually increased with the charging and discharging process, while for Bi_2S_3-rGO8 electrodes, the redox peaks almost stay constant after the 2^{nd} cycle. This indicates that the graphene composite improves the reversibility and cycling stability of Bi_2S_3 electrode, but the reversibility becomes worse with the increase of graphene content (Figure S10), which is consistent with the cycle and rate performance in Figure 2(a-c).

3.3 Performance enhancement and charge storage mechanisms

We first evaluated the pseudocapacitance behaviour of Bi_2S_3-rGO8 composites with fine and uniform Bi_2S_3 grain size. Figure 3(a) shows the cyclic voltammetry curves of the Bi_2S_3-RGO8 electrode at different scan rates of 0.2-1 mV s^{-1}. It is found that with the increase in scan rate, the oxidation peak gradually shifts to higher potential, and the reduction peak shifts to lower potential, accompanied by an increase of the peak current. The link between peak current (i) and scan rate (υ) can be described as follows [47,48]:

$$i = a\upsilon^b \qquad (1)$$

which can be also written as

$$\log(i) = b\log(\nu) + \log(a) \qquad (2)$$

where b is defined as the slope of the log (i) and log (v) curves. Generally, b is between 0.5 and 1. When the value of b reaches 0.5, the electrochemical process is dominated by ion diffusion, while for the values of b close to 1, the pseudo-capacitance effect dominates. Figure 3 (b) shows the relationship between log v and log i, and the b value of the redox peak can be obtained from the slope of the straight line. The b values of peaks 1 and peak 2 are 0.851 and 0.916 respectively, in Bi_2S_3-rGO8 electrodes. The fraction of pseudocapacitive contribution can be determined by the following equation:

$$i = k_1 v + k_2 v^{1/2} \qquad (3)$$

where $k_1 v$ represents the pseudocapacitance controlled process, and $k_2 v^{1/2}$ represents the ion diffusion controlled process. Figure 3(c) shows the pseudocapacitive contribution ratio of Bi_2S_3-rGO8 electrode at different scan rates. The percentage of pseudocapacitive contribution in the total capacity is 71.10%, 76.22%, 79.14%, 81.98%, and 84.87%, respectively. Interestingly, these values are close to the bare Bi_2S_3 and the other two Bi_2S_3-rGO composites as shown in Figure S11, which indicates that pseudocapacitive effect is not the main contributor to the enhanced performance of Bi_2S_3-rGO composites.

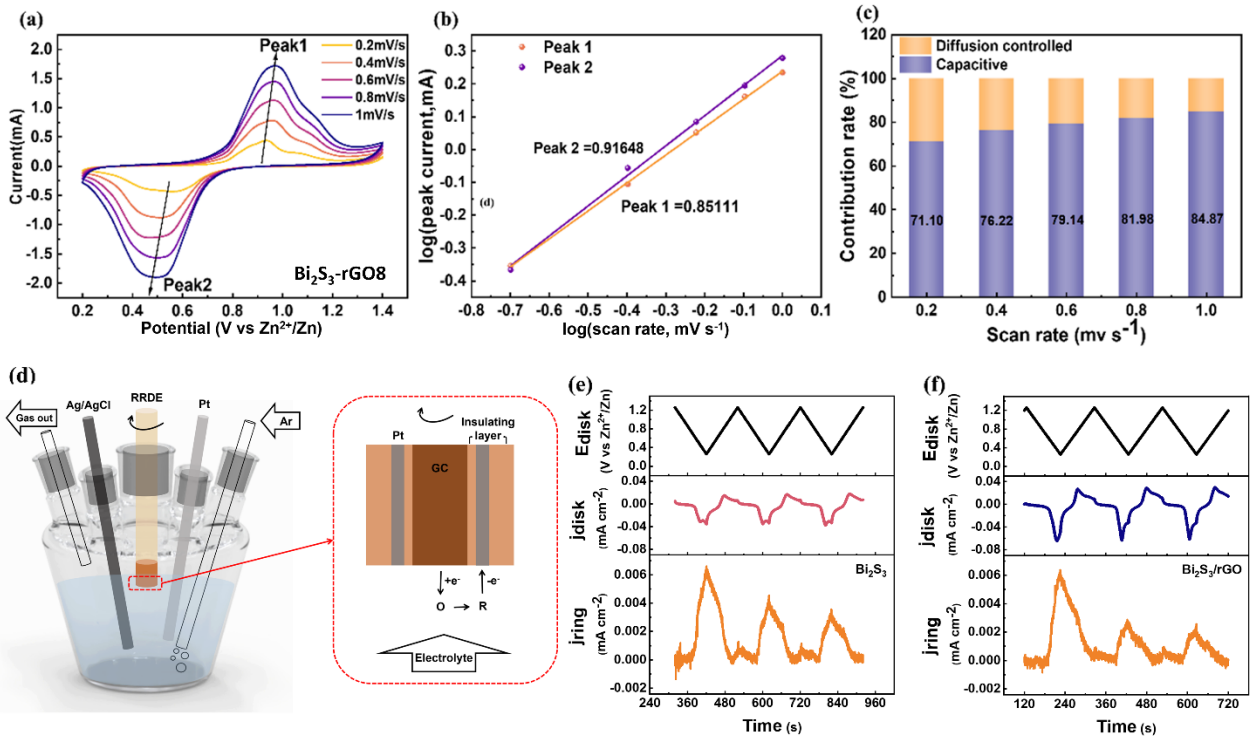

Figure 3. Electrochemical kinetics study of Bi_2S_3-rGO8 for zinc ion battery. (a) CVs at different scan rates, (b) relationship between log v and log i, (c) percentages of capacitance-controlled behaviour to the total capacity at various scan rates. (d) Sketch of the electrochemical cell for RRDE measurements, and disc potential, disc current and ring current as a function of time for (e) Bi_2S_3 and (f) Bi_2S_3-rGO8 during initial cyclic voltammograms (ring potential held at 0.1V vs

Ag/AgCl; disc scan rate, 10 mV s^{-1}).

We also performed rotating ring–disc electrode (RRDE) measurements to compare the electrode dissolution of Bi_2S_3 and Bi_2S_3-rGO8 during the initial CV scans, as materials stability under electrochemical conditions is a major factor in capacity fading [50, 51]. Figure 3d shows the experimental setup, in which a glassy carbon (GC) disc is coated uniformly with the electrode material under study (Bi_2S_3 or Bi_2S_3-rGO8). If, as a function of potential, this electrode material releases an electroactive species in solution, this is hydrodynamically transported to the Pt ring electrode surrounding the GC disc, where it can be detected by oxidation or reduction. While the potential of the disc and the overlayer are typically scanned, the ring potential is held at a value suitable for oxidation or reduction of the dissolving species. Under optimal conditions, and provided the dissolving species of interest is indeed electroactive, a standard RRDE setup as can be found in many electrochemistry labs can therefore provide real-time analysis and even chemical speciation of battery electrode dissolution—an important complement to inductively coupled plasma analysis [50].

Figure 3e,f shows the potential of Bi_2S_3 and Bi_2S_3-rGO8 coated on the glassy carbon (GC) disc electrode, which was scanned back and forth within the Zn intercalation/de-intercalation voltage range (~0.1-1.3 V vs Zn^{2+}/Zn). We note that for technical reasons, the scan rate here was 10 mV s^{-1}, that is, between one and two orders of magnitude faster than in the cyclic voltammograms shown in Figures 2d,e and 3a. The disc current density j_{disc} as a function of time in Figures 3e,f, however, shows all characteristics of the slower measurements (in particular the double peak feature in both cathodic and anodic scan direction, and systematically higher currents for Bi_2S_3-rGO8 than for Bi_2S_3), supporting the validity of our data. Based on the trend in Figure 3c and the discussion in the previous section, we can further infer that at a scan rate of 10 mV s^{-1}, virtually all current will be related to ion diffusion. During the potential scans of the disc, the potential of the Pt ring electrode was held at a constant value of 1.06V vs Zn^{2+}/Zn, and the ring current density j_{ring} is shown in the bottom panels of Figure 3e,f. Importantly, at the beginning of the shown cycles, both the disc and ring currents are close to zero, indicating that negligible Faradaic current flows at both electrodes and that no electroactive species is detected at the ring. As the disc potential is scanned in the negative direction, the ring current increases steeply, reaches a maximum when the scan direction is reversed, and approaches zero again at the end

of the cathodic half-cycle, indicating that the charging/discharging of the electrode material is associated with the release of a species in solution that can subsequently be oxidized at the ring.

In view of the fact that the element occurs as Bi(III) in Bi_2S_3 and that +III is the most common oxidation state, we hypothesise that the oxidation current at the ring originates from Bi^{3+} (aq) → Bi^{5+} (aq) $+2e^-$. This equation reflects only the change in the oxidation state of the element, as its hydrolysis is well known and may cause trivalent bismuth to exist as BiO^+ or $BiOH^{2+}$ [52]. A full elucidation of the nature of the dissolution at the disc electrode and of the identity of the electroactive species detected at the ring is beyond the scope of this article. However, the clear correlation between the features observed in the disc current and the magnitude of the ring current provides strong support for the appearance of Bi in the solution being related to the charging & discharging process of the electrode material.

During the anodic half-cycle, the ring current increases again, but remains limited to ten times lower values than during the cathodic half-cycle. Comparing the behaviour of Bi_2S_3 and Bi_2S_3-rGO8, we observe that during the first cycle, the ring currents are almost identical; subsequent cycles, however, show a significantly lower ring current—and hence dissolution at the disc—for Bi_2S_3-rGO8, in spite of the fact that the disc current for Bi_2S_3-rGO8 is systematically higher than for Bi_2S_3, which reflects the higher capacity of Bi_2S_3-rGO8. If we normalize the ring current for the electrochemical activity of the material on the disc, the difference in stability between the two materials becomes even more dramatic. According to the results of RRDE measurements, we believe that the covalent linkage of Bi_2S_3 to rGO provides strong interfacial coupling between Bi_2S_3 and rGO [49] and therefore increases the cycle stability by inhibiting the dissolution of electrode active materials.

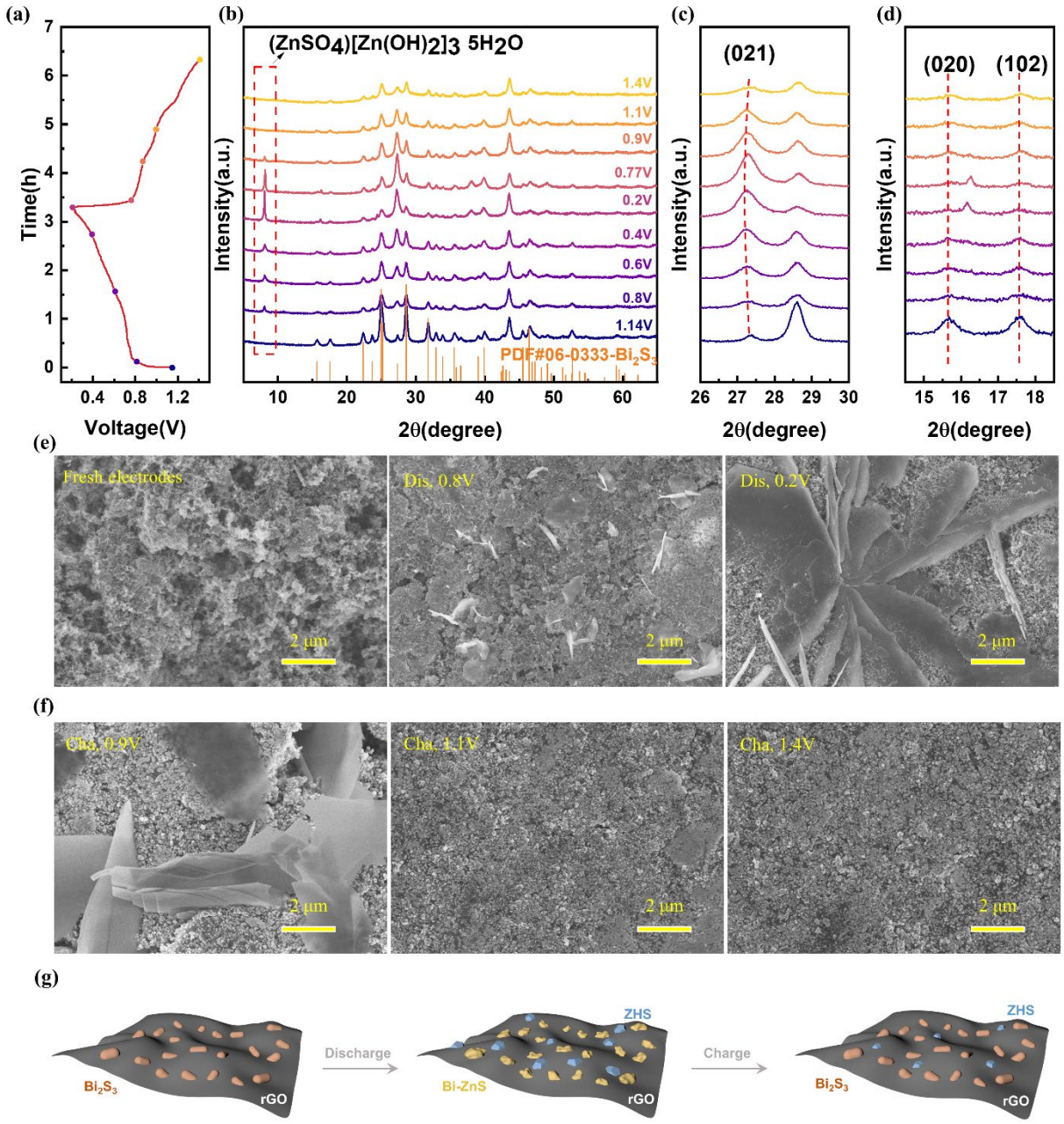

Figure 4. Ex-situ investigation of the discharge/charge process. (a) The charge/discharge profiles at 0.1 A g^{-1} with a series of selected points mark the electrode status for subsequent analysis. (b) *Ex-situ* XRD patterns of Bi_2S_3-rGO8 in different selected states and (c) (d) enlarged patterns of the (021) and (020) peaks of Bi_2S_3-rGO8. SEM characterization results of Bi_2S_3-rGO8 cathode during the first discharge (e) and charge (f) at different voltage states. (g) Schematic diagram of the phase conversion and surface reaction of Bi_2S_3-rGO electrode during the charge/discharge cycles.

To further study the zinc ion storage mechanism in electrodes, we used *ex-situ* XRD to characterize the structural evolution of electrode materials during the charge and discharge process. Figures 4(a-d) are the charge/discharge profiles and XRD patterns of the Bi_2S_3-rGO8 electrode in different charging

and discharging states during the first cycle, from which the changes in the crystal structure of the electrode can be revealed. As can be seen from the Figure 4(b), apart from the diffraction peaks of rhombic phase Bi_2S_3, the characteristic peak of $(ZnSO_4)[Zn(OH)_2]_3 \cdot 5H_2O$ (ZHS) [50,51] was also observed at ~ 2θ=8.093 degrees. This characteristic diffraction peak appears at the discharge of 0.8 V, and the diffraction peak intensity gradually increased to the maximum value at the last discharge state (0.2V). In the subsequent charging process, the diffraction peak intensity of ZHS gradually reduced and disappeared when the charging voltage reaches higher than 1.1 V. These results indicate that the formation/decomposition of ZHS is reversible upon the charge and discharge. Figure 4(c) shows the enlarged picture of the diffraction patterns between 2θ ~ 26-30 degrees. In the figure, the (021) diffraction peak shifts to a lower diffraction angle during the discharge process, while it shifts back to the original position in the charging process. Assuming this peak shifting is caused by the Zn^{2+} intercalation, the peak shifting should be also observed in the (020) plane which is also parallel to the *a*-axis of Bi_2S_3 crystal lattice. But the (020) peak in Figure 4(d) shows a typical conversion reaction behaviour: peak intensity is reduced during the discharge, and being increased during the charge, but there do not exist peak position shifting. Moreover, according to Bragg equation, the (021) peak position shifting corresponding to the interplanar spacing of Bi_2S_3 crystal plane ($d_{(021)}$) changes from an initial value of about 3.258 Å to 3.276 Å during the discharge (Figure S12). This tiny change (Δ=0.008 Å) cannot be attributed to the Zn^{2+} intercalation considering that the radius of Zn^{2+} is around 0.74 Å. We believe that this "fictitious" peak shifting is caused by the formation and disappearance of ZnS at around 2θ = 27.12 degrees. In other words, Bi_2S_3 stores zinc ions through the conversion reaction between Bi_2S_3 and ZnS. At the full discharge state, the Bi_2S_3-rGO8 can be almost fully conversed as ZnS and Bi^0, while a certain amount of unreacted Bi_2S_3 can be found in bare Bi_2S_3. The degree of completion of $Bi_2S_3 \leftrightarrow ZnS/Bi^0$ conversion reaction was dramatically increased because of not only the lower electrode polarization and smaller grain size introduced by rGO electronic conductive network, but also the enhanced charge transfer kinetics derived from the Bi-O-C heterostructure.

The reversible $(ZnSO_4)[Zn(OH)_2]_3 \cdot 5H_2O$ (ZHS) formation on the electrode surface was characterized using SEM. Figures 5(d) and (e) show the surface morphology of Bi_2S_3-RGO electrodes at different

charging and discharging states. As can be seen from the figures, ZHS micro/nanoflakes were observed on the electrode surface as the discharge process progressed [52]. With the decrease in discharge voltage, the number of nanosheets gradually increased and covered the electrode surface, while during the charging, the nanosheets begin to disappear gradually (Figures S13, S14). When charging at about 1.1V, the ZHS micro-sheets on the electrode surface almost disappear, which also proves the chemical reversibility of this process. This is consistent with the above *ex-situ* XRD results, in which the ZHS peaks reversibly appeared and disappeared in the spectra in Figure 4(b). Similar results were reported in other Cu_2S and manganese dioxide [50,51] based on the conversion reaction charge storage mechanism. The overall electrode phase conversion and surface reaction during the charge/discharge cycles are sketched and summarized in Figure 4(g).

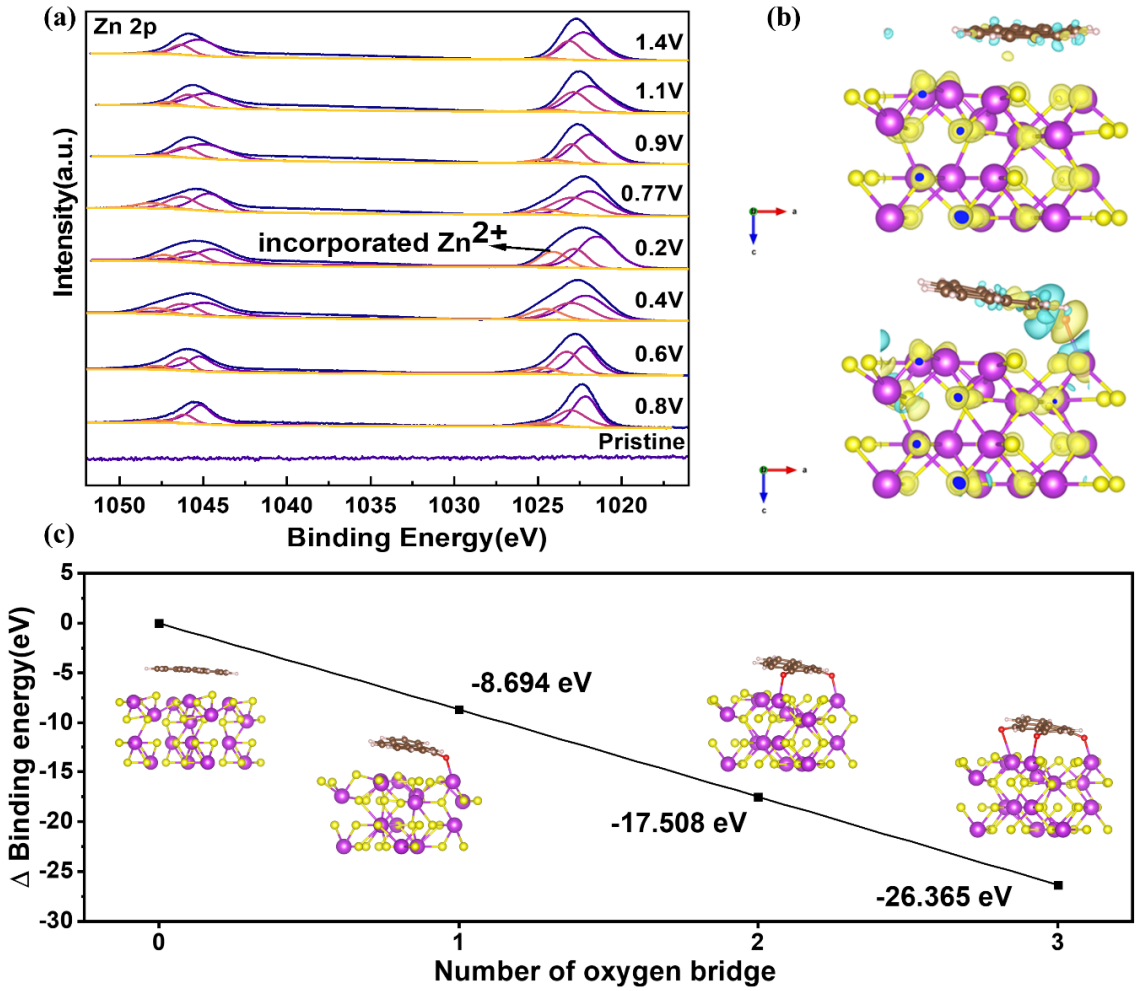

Figure 5. (a) XPS spectra of Zn2p on the surface of Bi_2S_3-rGO8 electrode under different charging and discharging states during the first charge-discharge cycle (The cells were cycled at a current density of 0.1A g^{-1}). (b) The charge density difference of the Bi_2S_3 and rGO without (up) and with (down) oxygen bridge. (c) The binding energy difference of

the Bi_2S_3 and rGO with increased oxygen bridge.

The reversible formation/decomposition of ZHS and the reaction mechanism between Zn and Bi_2S_3 were further studied by the *ex-situ* XPS spectra of Zn2p, as shown in Figure 5(a). The high-resolution spectra can be found in Figure S15. It can be seen from the figures that at the initial state, two pairs of Zn^{2+} peaks appear at 1021.4 eV/1044.3 eV and 1022.8 eV/1045.7 eV can be attributed to the Zn^{2+} peaks of $Zn(OH)_2$ and $ZnSO_4$ in ZHS, respectively, while the peaks at 1024.1 eV /1047.3 eV derive from the reduction product (ZnS) [45]. Importantly, it was found that the peak intensity of Zn^{2+} at 1024.1 and 1047.3 eV increased gradually during the discharge process, which unambiguously proves the formation of ZnS. The peak intensity decreased gradually during the charging process, corresponding to the extraction of Zn^{2+} from the ZnS. This result confirms that the conversion reaction ($Bi_2S_3 + 3Zn \leftrightarrow 3ZnS + 2Bi$) is chemically reversible, which is consistent with the *ex-situ* XRD result in Figure 4.

3.4 The critical role of oxygen bridges in conversion-based Zn storage Bi_2S_3 cathode

The fracturing of electrode micro/nanostructures and dissolution of metal elements are the primary issue of conversion mechanism-based electrode material. The volume changes caused by replacing Bi with Zn in Bi_2S_3 during the first discharge may completely destruct the pristine Bi_2S_3 structures. However, in the Bi_2S_3/rGO composite electrode, the strongly bonded Bi with graphene substrate could effectively inhibit the damage of the electrode structures and Bismuth dissolution, as well as enhance the charge transfer and mitigate active material dissolution in Bi_2S_3/rGO composite. We further used Density Functional Theory (DFT) calculations to evaluate the charge transfer and structure stabilization of Bi-O-C structure in Bi_2S_3/rGO composite as shown in Figures 5(b) and (c). Figure 5(b) shows the two scenarios of the charge-density difference of a Bi_2S_3 and graphene interface without (up) and with (down) an oxygen bridge formed between them. The first scenario happens in many traditional physical synthesized Bi_2S_3 and graphene composites, such as ball milling. There aren't any covalence bonds formed between two materials, the charge hopping between two materials is intrinsically inhibited. However, in the second scenario where an oxygen bridge is introduced during the hydrothermal synthesize process, it can be seen that because of the linkage between Bi and O atoms, the large electron charge overlaps in the interface between the Bi_2S_3 and graphene provides a good

pathway for electron transport. The conversion reaction between zinc ions and Bi_2S_3 can therefore be promoted by the rapid charge compensation of electrons flowing through the oxygen bridge. More importantly, as shown in Figure 5(c), we also found that the binding energy of the modelled graphene/Bi_2S_3 system decreases with the increase of the number of oxygen bridges. For each additional oxygen bridge, the system binding energy decreased by about 9 eV. This result suggested that oxygen bridges promote the coupling between rGO and Bi_2S_3. The strongly anchored bismuth on the graphene through a Bi-O-C bridge allows a highly reversible conversion reaction. The easy binding/difficult dissociation characteristic of Bi adatoms on the oxygenated graphene not only facilitates fast electron hopping from graphene to Bi_2S_3, but also prevents the pulverization of Bi_2S_3 micro/nanostructures and dissolution of Bismuth into the electrolyte. Therefore, combined with the *ex-situ* XRD, SEM, RRDE and XPS characterizations, we ascribe the enhanced electrochemical performance and charge storage in the Bi_2S_3/rGO composite to the robust rGO conductive network and strong interfacial coupling effect. A similar scenario was recently observed in an enhanced oxygen evolution reaction on a covalently linked graphene/metal-organic framework composite [57].

4. Conclusions

Bismuth sulfide combined with different contents of rGO additive was synthesized by hydrothermal reaction. Detailed structural characterization shows that the reduced graphene oxide serves as the nucleation substrate enabling the formation of fine and uniform-sized Bi_2S_3 grains. The rGO substrate forms chemical bonds with bismuth through oxygen bridges in the composite material, and the strongly anchored bismuth on the graphene allows a highly reversible conversion reaction. The easy binding/difficult dissociation characteristic of Bi adatoms on the oxygenated graphene facilitates fast electron hopping between rGO and Bi_2S_3, and enhances the electrochemical stability of the electrode by mitigating the dissolution of Bi_2S_3 active material. It was found that optimizing the GO composite can improve the electrochemical properties of Bi_2S_3. The specific capacity of Bi_2S_3-rGO8 composite material is ~186 mAh g^{-1} at a current density of 500 mA g^{-1} after 150 cycles, which is much higher than the value (~10 mAh g^{-1}) of bare Bi_2S_3 electrode without rGO. Additionally, the Bi_2S_3 nucleated on GO with smaller particle sizes shortens the transport path of zinc ions, which is again beneficial for fast charge transfer. Therefore, Bi_2S_3-rGO8 can even deliver more than 100 mAh g^{-1} at 10 A/g charge/discharge current density. This is the best rate performance of Bi_2S_3 to the best of our knowledge

so far as shown in the comparation plot in Figure S16(a) of supplementary information, but the cycle stability of our Bi_2S_3-rGO with optimized mass loading (Figure S17) is not the outstanding among them (see Figure S16b) and needs further improvement. Furthermore, the Zinc storage mechanism of Bi_2S_3-rGO composite was analyzed by XRD and XPS, which indicates that the charging mechanism of Zn/Bi_2S_3-rGO is based on the reversible conversion reaction of Zn^{2+} in Bi_2S_3-rGO framework. During the discharge process, Zn^{2+} is embedded in Bi_2S_3-rGO frame to form ZnS and Bi^0 wrapped in rGO. The process is accompanied by the formation of ZHS on the electrode surface. During the charging process, Zn^{2+} escapes from ZnS/Bi^0 mixture confined by the rGO frame, and ZHS gradually disappears. We believe that our detailed understanding of Bi_2S_3-rGO electrode charge storage mechanisms can help to design analogous composite materials with good Zn^{2+} storage performance, fast reaction kinetics, and high capacity.

Lastly, although the fabrication cost (~ 419 \$ kWh^{-1}, see Table S1 in supplementary information) of our labscale Bi_2S_3-rGO8 ZIBs is comparable to the reported high-temperature Na–S batteries (~445–555 \$ kWh^{-1}) [58], vanadium redox flow batteries (~550 \$ kWh^{-1}) and Ni-Cd batteries (~200-400 \$ kWh^{-1}) [59, 44], it is still higher than other state-of-the-art energy technologies currently commercialized like Li-ion batteries (~170-250 \$ kWh^{-1}) [60, 61], Ni-MH batteries (~198 \$ kWh^{-1}) [62] and Pb-acid batteries (~ 166 \$ kWh^{-1}). However, we should stress that the fabrication of ZIB does not require an oxygen and moisture-free environment, which could further reduce the cost of scaling up. Additionally, with the growth of the global graphene industry, the price of GO is expected to be further reduced in the future. This could also contribute to the synthesis cost of cathode material and reduce the total cost of our ZIBs, which has the potential to be used as a large-scale storage device electrode in the future.

Acknowledgements

The authors wish to acknowledge the financial support by the National Natural Science Foundation of China (No. 61574037, 11874113, 11344008, 11204038, 22179020), Foreign science and technology cooperation project of Fuzhou Science and Technology Bureau (No. 2021-Y-086), Industry-university Cooperation Project of Fujian Province (No. 2020H06027), the Faraday Institution (grant number FIRG018), and EPSRC project EP/V00767X/1. DZ acknowledges the receipt of a Sydney Andrew Scholarship from the Society of Chemical Industry.

References

[1] Armand, M.; Tarascon, J.-M. Building Better Batteries. Nature **2008**, 451, 652-657.

[2] Dunn, B.; Kamath, H.; Tarascon, J.-M. Electrical Energy Storage for the Grid: A Battery of Choices. Science **2011**, 334, 928-935.

[3] Xu, W.; Zhao, K.; Wang, Y. Electrochemical Activated Moo2/Mo2n Heterostructured Nanobelts as Superior Zinc Rechargeable Battery Cathode. Energy Stor. Mater. **2018**, 15, 374-379.

[4] Scrosati, B.; Hassoun, J.; Sun, Y.-K. Lithium-Ion Batteries. A Look into the Future. Energy Environ. Sci. **2011**, 4, 9, 3287–3295.

[5] Yang, Z.; Zhang, J.; Kintner-Meyer, M. C. W.; Lu, X.; Choi, D.; Lemmon, J. P.; Liu, J. Electrochemical Energy Storage for Green Grid. Chem. Rev. **2011**, 111, 5, 3577-3613.

[6] Chevrier, V. L.; Ceder, G. Challenges for Na-Ion Negative Electrodes. J. Electrochem. Soc. **2011**, 158, 9, A1011-A1014.

[7] Li, Z.; Wu, L.; Dong, S.; Xu, T.; Li, S.; An, Y.; Jiang, J.; Zhang, X. Pencil Drawing Stable Interface for Reversible and Durable Aqueous Zinc - Ion Batteries. Adv. Funct. Mater. **2020**, 31, 4, 2006495.

[8] Long, J.; Yang, Z.; Yang, F.; Cuan, J.; Wu, J. Electrospun Core-Shell Mn3o4/Carbon Fibers as High-Performance Cathode Materials for Aqueous Zinc-Ion Batteries. Electrochim. Acta **2020**, 344, 136155.

[9] Zhang, Y.; Deng, S.; Li, Y.; Liu, B.; Pan, G.; Liu, Q.; Wang, X.; Xia, X.; Tu, J. Anchoring Mno2 on Nitrogen-Doped Porous Carbon Nanosheets as Flexible Arrays Cathodes for Advanced Rechargeable Zn–Mno2 Batteries. Energy Stor. Mater. **2020**, 29, 52-59.

[10] Tan, Q.; Li, X.; Zhang, B.; Chen, X.; Tian, Y.; Wan, H.; Zhang, L.; Miao, L.; Wang, C.; Gan, Y.; Jiang, J.; Wang, Y.; Wang, H. Valence Engineering Via in Situ Carbon Reduction on Octahedron Sites Mn3o4 for Ultra-Long Cycle Life Aqueous Zn-Ion Battery. Adv. Energy Mater. **2020**, 10, 38, 2001050.

[11] Wu, S.; Ding, Y.; Hu, L.; Zhang, X.; Huang, Y.; Chen, S. Amorphous V2O5 as High Performance Cathode for Aqueous Zinc Ion Battery. Mater. Lett. **2020**, 277, 128268.

[12] Zhang, X.; Tang, Y.; He, P.; Zhang, Z.; Chen, T. Edge-Rich Vertical Graphene Nanosheets Templating V2o5 for Highly Durable Zinc Ion Battery. Carbon **2021**, 172, 207-213.

[13] Liao, M.; Wang, J.; Ye, L.; Sun, H.; Wen, Y.; Wang, C.; Sun, X.; Wang, B.; Peng, H. A Deep-Cycle Aqueous Zinc-Ion Battery Containing an Oxygen-Deficient Vanadium Oxide Cathode. Angew. Chem.

Int. Ed. **2020**, 59, 6, 2273-2278.
[14] Fang, G.; Zhou, J.; Pan, A.; Liang, S. Recent Advances in Aqueous Zinc-Ion Batteries. ACS Energy Lett. **2018**, 3, 10, 2480-2501.
[15] Geng, L.; Lv, G.; Xing, X.; Guo, J. Reversible Electrochemical Intercalation of Aluminum in Mo6s8. Chem. Mater. **2015**, 27, 14, 4926-4929.
[16] Hu, Z.; Liu, Q.; Chou, S. L.; Dou, S. X. Advances and Challenges in Metal Sulfides/Selenides for Next-Generation Rechargeable Sodium-Ion Batteries. Adv. Mater **2017**, 29, 48
[17] Xiong, T.; Wang, Y.; Yin, B.; Shi, W.; Lee, W. S. V.; Xue, J. Bi2S3 for Aqueous Zn Ion Battery with Enhanced Cycle Stability. Nanomicro Lett. **2019**, 12, 1, 8.
[18] Li, S.; Liu, Y.; Zhao, X.; Cui, K.; Shen, Q.; Li, P.; Qu, X.; Jiao, L. Molecular Engineering on MoS2 Enables Large Interlayers and Unlocked Basal Planes for High-Performance Aqueous Zn-Ion Storage. Angew. Chem. Int. Ed. **2021**, 60, 37, 20286-20293.
[19] Ren, Z.; Sun, Y.; Yin, Y.; Zhang, J.; Ren, X.; Zhao, Y.; Liang, Z.; Huai, P.; Song, F.; Jiang, Z.; Wen, W.; Li, X.; Tai, R.; Zhu, D. Metallic V5s8 Microparticles with Tunnel-Like Structure for High-Rate and Stable Zinc-Ion Energy Storage. Energy Stor. Mater. **2021**, 42, 786-793.
[20] Li, W.; Jing, X.; Ma, Y.; Chen, M.; Li, M.; Jiang, K.; Wang, D. Phosphorus-Doped Carbon Sheets Decorated with Ses2 as a Cathode for Aqueous Zn-Ses2 Battery. Chem. Eng. J. **2021**, 420, 129920.
[21] Ni, J.; Zhao, Y.; Liu, T.; Zheng, H.; Gao, L.; Yan, C.; Li, L. Strongly Coupled Bi2s3@Cnt Hybrids for Robust Lithium Storage. Adv. Energy Mater. **2014**, 4, 16, 1400798.
[22] Liang, H.; Ni, J.; Li, L. Bio-Inspired Engineering of Bi2s3-Ppy Yolk-Shell Composite for Highly Durable Lithium and Sodium Storage. Nano Energy **2017**, 33, 213-220.
[23] Zhao, Y.; Ma, L.; Zhu, Y.; Qin, P.; Li, H.; Mo, F.; Wang, D.; Liang, G.; Yang, Q.; Liu, W.; Zhi, C. Inhibiting Grain Pulverization and Sulfur Dissolution of Bismuth Sulfide by Ionic Liquid Enhanced Poly(3,4-Ethylenedioxythiophene):Poly(Styrenesulfonate) for High-Performance Zinc-Ion Batteries. ACS Nano **2019**, 13, 6, 7270-7280.
[24] Sun, X.; Wang, L.; Li, C.; Wang, D.; Sikandar, I.; Man, R.; Tian, F.; Qian, Y.; Xu, L. Dandelion-Like Bi2s3/Rgo Hierarchical Microspheres as High-Performance Anodes for Potassium-Ion and Half/Full Sodium-Ion Batteries. Nano Res. **2021**, 14, 12, 4696-4703.
[25] Yang, W.; Wang, H.; Liu, T.; Gao, L. A Bi2s3@Cnt Nanocomposite as Anode Material for Sodium Ion Batteries. Mater. Lett. **2016**, 167, 102-105.

[26] Lu, C.; Li, Z.; Yu, L.; Zhang, L.; Xia, Z.; Jiang, T.; Yin, W.; Dou, S.; Liu, Z.; Sun, J. Nanostructured Bi2s3 Encapsulated within Three-Dimensional N-Doped Graphene as Active and Flexible Anodes for Sodium-Ion Batteries. Nano Res. **2018**, 11, 9, 4614-4626.

[27] Liu, Y.; Jiao, L.; Wu, Q.; Zhao, Y.; Cao, K.; Liu, H.; Wang, Y.; Yuan, H. Synthesis of Rgo-Supported Layered Mos2 for High-Performance Rechargeable Mg Batteries. Nanoscale **2013**, 5, 20, 9562–9567.

[28] Blöchl, P. E. B. Projector Augmented-Wave Method. Phys. Rev. B **1994**, 50, 24, 17953-17979.

[29] Kresse, G.; Hafner, J. Ab Initio Molecular Dynamics for Open-Shell Transition Metals. Phys. Rev. B **1993**, 48, 17, 13115-13118.

[30] Kresse, G.; Furthmüller, J. Efficient Iterative Schemes for Ab Initio Total-Energy Calculations Using a Plane-Wave Basis Set. Phys. Rev. B **1996**, 54, 11169.

[31] Perdew, J. P.; Burke, K.; Ernzerhof, M. Generalized Gradient Approximation Made Simple. Phys. Rev. Lett. **1996**, 77, 3865.

[32] Monkhorst, H. J.; Pack, J. D. Special Points for Brillouin-Zone Integrations. Phys. Rev. B **1976**,

[33] Klimeš, J.; Bowler, D. R.; Michaelides, A. Chemical Accuracy for the Van Der Waals Density Functional. J. Phys-Condens Mat. **2010**, 22, 2, 022201.

[34] Zhu, L.; Yang, C.; Chen, Y.; Wang, J.; Wang, C.; Zhu, X. Lithium Storage Performance and Mechanism of Vs4/Rgo as an Electrode Material Associated with Lithium-Sulfur Batteries. J. Alloys Compd. **2019**, 785, 855-861.

[35] Dong, Y.; Hu, M.; Zhang, Z.; Zapien, J. A.; Wang, X.; Lee, J.-M. Hierarchical Self-Assembled Bi2s3 Hollow Nanotubes Coated with Sulfur-Doped Amorphous Carbon as Advanced Anode Materials for Lithium Ion Batteries. Nanoscale **2018**, 10, 28, 13343-13350.

[36] Chen, Y.; Tian, G.; Mao, G.; Li, R.; Xiao, Y.; Han, T. Facile Synthesis of Well-Dispersed Bi2s3 Nanoparticles on Reduced Graphene Oxide and Enhanced Photocatalytic Activity. Appl. Surf. Sci. **2016**, 378, 231-238.

[37] Tian, M.; Liu, C.; Neale, Z. G.; Zheng, J.; Long, D.; Cao, G. Chemically Bonding Nife-Ldh Nanosheets on Rgo rGO for Superior Lithium-Ion Capacitors. ACS Appl. Mater. Interfaces **2019**, 11, 39, 35977-35986.

[38] Liu, Y.; Li, M.; Zheng, Y.; Lin, H.; Wang, Z.; Xin, W.; Wang, C.; Du, F. Boosting Potassium-Storage Performance Via the Functional Design of a Heterostructured Bi2S3@Rgo rGO Composite.

Nanoscale **2020**, 12, 48, 24394-24402.

[39] Zhou, G.; Wang, D.-W.; Yin, L.-C.; Li, N.; Li, F.; Cheng, H.-M. Oxygen Bridges between Nio Nanosheets and Graphene for Improvement of Lithium Storage. ACS Nano **2012**, 6, 4, 3214–3223.

[40] Gote, G. H.; Bhopale, S. R.; More, M. A.; Late, D. J. Realization of Efficient Field Emitter Based on Reduced Graphene Oxide-Bi2s3 Bi2S3 Heterostructures. Phys Status Solidi (a) **2019**, 216, 18, 1900121.

[41] Lu, H.; Guo, Q.; Zan, F.; Xia, H. Bi2s3 Nanoparticles Anchored on Graphene Nanosheets with Superior Electrochemical Performance for Supercapacitors. Mater. Res. Bull. **2017**, 96, 471-477.

[42] García-Peña, N.-G.; Díaz, D.; Rodríguez-Gattorno, G.; Betancourt, I.; Zumeta-Dubé, I. Facile Synthesis of Rod-Shaped Bismuth Sulfide@Graphene Oxide (Bi2S3@Go) Composite. Mater. Chem. Phys. **2018**, 219, 376-389.

[43] Wan, F.; Zhang, L.; Dai, X.; Wang, X.; Niu, Z.; Chen, J. Aqueous Rechargeable Zinc/Sodium Vanadate Batteries with Enhanced Performance from Simultaneous Insertion of Dual Carriers. Nat. Commun. **2018**, 9, 1, 1656.

[44] R. Wang, M. Shi, L. Li, Y. Zhao, L. Zhao, C. Yan In-Situ Investigation and Application of Cyano-Substituted Organic Electrode for Rechargeable Aqueous Na-Ion Batteries. Chemical Engineering Journal **2023**, 451.

[45] C. Chen, H. Zhu, M. Shi, L. Hu, Z. Xue, H. Ye, L. Zhao, C. Yan Oxygen Vacancies-Modulated Tungsten Oxide Anode for Ultra-Stable and fast aqueous Aluminum-Ion Storage. Energy Storage Materials **2022**, 49, 370-379.

[46] Liu, W.; Liu, P.; Hao, R.; Huang, Y.; Chen, X.; Cai, R.; Yan, J.; Liu, K. One-Dimensional MnO2 Nanowires Space-Confined in Hollow Mesoporous Carbon Nanotubes for Enhanced Zn2+ Storage Performance. Chem. Electro. Chem. **2020**, 7, 5, 1166-1171.

[47] Huang, X. H.; Wang, C. B.; Zhang, S. Y.; Zhou, F. Cuo/C Microspheres as Anode Materials for Lithium Ion Batteries. Electrochim. Acta **2011**, 56, 19, 6752-6756.

[48] Chao, D.; Liang, P.; Chen, Z.; Bai, L.; Shen, H.; Liu, X.; Xia, X.; Zhao, Y.; Savilov, S. V.; Lin, J.; Shen, Z. X. Pseudocapacitive Na-Ion Storage Boosts High Rate and Areal Capacity of Self-Branched 2d Layered Metal Chalcogenide Nanoarrays. ACS Nano **2016**, 10, 11, 10211-10219.

[49] Niu, F.; Yang, J.; Wang, N.; Zhang, D.; Fan, W.; Yang, J.; Qian, Y. Mose2-Covered N,P-Doped Carbon Nanosheets as a Long-Life and High-Rate Anode Material for Sodium-Ion Batteries. Adv.

Funct. Mater. **2017**, 27, 23, 1700522.

[50] Nikman, S.; Zhao, D.; Gonzalez-Perez, V.; Hoster, H. E.; Mertens, S. F. L. Surface or Bulk? Real-time Manganese Dissolution Detection in a Lithium-ion Cathode, Electrochimica Acta **2021**, 386, 138373.

[51] Tapia-Ruiz N. et al. Roadmap on Sodium Ion Batteries. Journal of Physics: Energy **2021**, 3, 031503.

[52] Swift, E.H. J. Am. Chem. Soc. **1923**, 45, 371-377

[53] Sun, J.; Tu, W.; Chen, C.; Plewa, A.; Ye, H.; Oh, J. A. S.; He, L.; Wu, T.; Zeng, K.; Lu, L. Chemical Bonding Construction of Reduced Graphene Oxide-Anchored Few-Layer Bismuth Oxychloride for Synergistically Improving Sodium-Ion Storage. Chem. Mater. **2019**, 31, 18, 7311-7319.

[54] Peng, Q.; Zhang, S.; Yang, H.; Sheng, B.; Xu, R.; Wang, Q.; Yu, Y. Boosting Potassium Storage Performance of the Cu2s Anode Via Morphology Engineering and Electrolyte Chemistry. ACS Nano **2020**, 14, 5, 6024-6033.

[55] Huang, J.; Wang, Z.; Hou, M.; Dong, X.; Liu, Y.; Wang, Y.; Xia, Y. Polyaniline-Intercalated Manganese Dioxide Nanolayers as a High-Performance Cathode Material for an Aqueous Zinc-Ion Battery. Nat. Commun. **2018**, 9, 1, 2906.

[56] Lin, C.; Chen, Y.; Zhang, W.; Li, J.; Lin, Y.; Kolosov, O. V.; Huang, Z. Recycling Spent Lead Acid Batteries into Aqueous Zinc-Ion Battery Material with Ultra-Flat Voltage Platforms. Ceram. Int. **2022**, 48, 18, 2580.

[57] Li, Z.; Guo, Y.; Li, K.; Wang, S.; De Bonis, E.; Cao, H.; Mertens, S. F. L.; Teng, C. Shape control of bimetallic MOF/graphene composites for efficient oxygen evolution reaction. J. Electroanal. Chem. **2023**, 930, 117114.

[58] Y. E. Durmus, H. Zhang, F. Baakes, G. Desmaizieres, H. Hayun, L. Yang, M. Kolek, V. Küpers, J. Janek, D. Mandler, S. Passerini, Y. Ein-Eli Side by Side Battery Technologies with Lithium-Ion Based Batteries. Advanced Energy Materials **2020**, 10, 24.

[59] Inamuddin I . Rechargeable Batteries: History, Progress and Applications. **2020**.

[60] Z. P. Cano, D. Banham, S. Ye, A. Hintennach, J. Lu, M. Fowler, Z. Chen Batteries and Fuel Cells for Emerging Electric Vehicle Markets. Nature Energy **2018**, 3, 4, 279-289.

[61] X. N. Penisa, M. T. Castro, J. D. A. Pascasio, E. A. Esparcia, O. Schmidt, J. D. Ocon Projecting

the Price of Lithium-Ion Nmc Battery Packs Using a Multifactor Learning Curve Model. Energies **2020**, 13, 20.

[62] O. Schmidt, A. Hawkes, A. Gambhir, I. Staffell The Future Cost of Electrical Energy Storage Based on Experience Rates. Nature Energy **2017**, 2, 8.